# Development of new types of bolted joints for cold-formed steel moment frame buildings

Lingfeng Yin[a,b], Yu Niu[a], Guan Quan[c]*, Han Gao[a], Jun Ye[d]

a School of civil engineering, Southeast University, Nanjing 211189, China
b School of engineering, Tibet University, Lhasa 850011, China
c School of Civil Engineering and Surveying, University of Portsmouth, Portsmouth PO1 3AH, UK
d Department of Civil & Environmental Engineering, University of Strathclyde, Glasgow G1 1XJ, UK
Corresponding author: guan.quan@port.ac.uk

**Abstract**

It has been a growing trend to use cold-formed steel (CFS) sections as primary structural members in low to multi-story buildings due to their high strength-to-weight ratios, ease of construction and flexibility in manufacturing to a variety of cross-sectional shapes. However, CFS frames are not widely used in seismic regions; one important reason is that the less redundant CFS joints generally have low ductility and energy dissipation capacity due to their inherently thin-walled properties. To address this issue, this paper presents an experimental programme and the corresponding results on two types of beam-to-column CFS joints, which are assembled to the two adjacent surfaces of the built-up CFS column in this paper. Different from the previous research, the two types of joints proposed are potentially suitable to connect CFS members in T-, L- and cruciform joints for multi-story framed-structure buildings. It was observed from the tests that the beams buckled before the occurrence of obvious damage to the tested joints. The two types of joints satisfied the seismic design philosophy of 'strong connection-weak beam'. Joint Type 2 (JT2) exhibits overall higher performance in terms of strength, ductility, and energy dissipation capacity than the Joint Type 1 (JT1). JT1 satisfies the rotational requirement for Ordinary Moment Frames (OMFs) while JT2 satisfies the rotational requirement for Special Moment Frames (SMFs), as defined in AISC Seismic Provisions. The connection zones within both joints can be classified as semi-rigid according to the approach recommended by Eurocode 3: Part 1-8, with JT1 exhibiting higher stiffness than JT2. Overall, the proposed two joints connected with very slender beams and less bolts, have so far shown moderate performance to provide resistance and ductility to be applied in CFS framed buildings in seismic regions, which can be improved in further work.

**Keywords:** Cold-formed steel connections; Moment-resisting frames; Cyclic tests; Seismic behaviour

## Introduction

Cold-formed steel (CFS) is commonly employed either as primary structural elements in shear wall systems [1][2] or as secondary structural elements such as in roof purlins [3][4] and storage racking [5][6], etc. The 19th century has seen



This is a peer-reviewed, accepted author manuscript of the following article: Yin, L., Niu, Y., Quan, G., Gao, H., & Ye, J. (2022). Development of new types of bolted joints for cold-formed steel moment frame buildings. Journal of Building Engineering , 50, [104171]. https://doi.org/10.1016/j.jobe.2022.104171

a growing trend to use CFS sections as primary structural members in low to multi-story buildings [7] and portal frames [8]-[11] due to their advantages of high strength-to-weight ratio, ease and speedy of construction and flexibility in manufacturing to a variety of cross-sectional shapes [12][13], etc. However, currently, the CFS sections are mostly used in low-to-multi-story buildings in regions with low seismic actions. This is because that the inherent premature buckling phenomenon of thin-walled sections [14][15] and the insufficient ductility and energy dissipation ability of the CFS moment joints [16][17] require the CFS members and joints to be more redundantly and rationally designed before being employed as the primary load-bearing components of structures in zones with high seismicity. However, the CFS design guidance [18][19] only recommends the design approach of individual fasteners, not the actual connections, due to the lack of relevant research. Therefore, investigation on the mechanical behaviour, including stiffness, strength, ductility and energy dissipation ability of CFS members and connections under cyclic load is in high demand to guide the earthquake resistant design of the CFS structures. It is worth noting that the mechanical behaviours of the CFS connections are often influenced by their connected columns and beams, and vice versa. Thus, the term CFS joint in this paper includes the CFS connection and its connected columns and beams adjacent to the connection.

Uang et al. [20] tested nine full-scale beam-column moment connections under cyclic load to support the development of design provisions for a lateral load resisting system in the AISI S110: Standard for Seismic Design of Cold-Formed Steel Structural Systems—Special Bolted Moment Frames (SBMFs). The research concluded that the beams and columns should be designed to maintain their elasticity, while frame energy dissipation should rely on bolt slippage and bearing in the moment connections. Phan et al. [21] considered the effect of bi-moment when calculating the ultimate flexural strength of CFS bolted moment connections using the effective width method in Eurocode 3 [22]. The predicted results from their proposed equations agree well with experimental and numerical data. Sabbagh et al. [17] carried out numerical investigation on the potential use of CFS sections in moment-resisting frames (MRFs) for seismic applications. The research indicated that by using curved flange beam sections, the local buckling failure of beams can be delayed. Also, the CFS connections can obtain sufficient strength and ductility if appropriately detailed and stiffened to allow the development of plasticity in the beams. Based on the findings of the research above, Sabbagh et al. [14] further conducted an experimental study on CFS joints and concluded that the application of a well-designed full configuration of stiffeners results in significant increases in joint ductility, moment capacity, and hysteretic energy dissipation capacity. Papargyriou et al. [23] numerically developed two new connections which engaged the flanges in the connection behaviour. Practical seismic design recommendations, which allow a balance between the load carrying

capacity of the connections and their seismic performance to be reached, were presented. Mojtabaei et al. [24] studied local buckling failure adjacent to the moment-resisting bolted connections in CFS back-to-back channel beams. The effects of a number of variables, such as the cross-sectional shape, the thickness of the beam, the bolt group configuration, and the bolt group length were investigated. Lee et al. [25] carried out numerical studies on the behaviour of top-seat flange cleat connections, which aimed to connect primary load bearing members in low and medium rise cold-formed steel buildings. Tan et al. [26] conducted experimental investigation on slip-in connections for cold-formed steel double channel sections. The research investigated the moment resistance of the proposed connections and concluded that the proposed connections could be classified as partial strength connections. Ye et al. [27] presented a comprehensive parametric study to discuss the effects of bolt arrangement, cross-sectional shape, gusset plate thickness and cross-sectional slenderness on the seismic performance of the CFS connections, proposed by Sabbagh et al. [14], under cyclic load. The research also conducted research on the simulation and behaviour of new types of joints with the emphasis on bolt pretension and slippage. Ye et al. [28] later proposed a design solution to provide the CFS joint with a bolt friction-slip mechanism to improve the joint energy dissipation capacity and ductility under cyclic load. Sato and Uang [29] concluded that the bolt slippage and bearing action can benefit the CFS joint with higher ductility and energy dissipation capacity. The research observed that their tested portal frames had sufficient lateral sway capacity to be classified as SMFs in AISC 341-16 [30]. Several numerical approaches [31][32][33] were also developed to meet the challenge of high nonlinearity of the connection behaviours, the complex interaction between the CFS members and fasteners, and a large number of fasteners in the modelling of CFS joints. Through the reviewed literature above, it can be found that there is still limited test result reported on the moment joint of CFS construction under cyclic load, apart from the tests on CFS joint with gusset plates conducted by Sabbagh et al. [14].

In this research, experiments have been carried out on two new types of CFS joints under cyclic loading. Compared with the well-studied CFS joint type by Sabbagh et al. [14], the new types of CFS joints introduced in this paper are designed to connect extensive types of CFS beam and column built-up sections. Moreover, the nature that less bolts are used in the proposed joints makes them more structurally sustainable and constructionally efficient. The tested joints in this paper are also connected by both cold-formed steel columns and cold-formed steel beams which are evaluated in the aspects of strength and ductility, rigidity and energy dissipation capacity. This research aims to explore the behaviours, including the mechanical properties and failure modes, of new types of CFS beam-to-column joints that are suitable for connecting different surfaces of the built-up CFS column sections in frame structures. It also aims to extend the

understanding of CFS joints under cyclic loading as well as to provide supplements to the database for CFS joint simulation under cyclic load.

## 1. Details of the proposed joints

In this section, two new types of CFS joints, which are designed to assemble the adjacent surfaces of the built-up CFS column in a new type of CFS framed building system, are introduced. The schematic diagram of the proposed cold-formed steel frame structure system is presented in Fig. 1 (a). The new CFS structure system is composed of build-up columns and build-up beams as the main load-bearing and lateral force resisting components. The framed built-up section is proposed to be used in a new type of CFS column, which is composed of four cold-formed steel plates with intermediate stiffeners that are connected by bolts. There are two types of built-up beam sections in the frame system. The first type of beam section (Beam I) is a built-up closed cross-section that is assembled by welding two identical Σ sections at their lip to flange intersections. The second type of beam section (Beam II) is a built-up open cross-section that is assembled by bolting two identical back-to-back Σ sections with intermediate stiffeners. The shape of the two beam cross-sections can be seen in Fig. 1 (a). The two beam types are connected to the adjacent column surfaces with different types of joints, as shown in Fig. 1 (b). Internal cruciform gusset plate is inserted in the joint area of the frame column, as shown in Fig. 2, to enhance the localized capacity of the column and to better transfer the applied loading from the adjacent beams to the column. The proposed CFS structure system is currently in the concepted design stage with industry partners, and will be applied to practical CFS structures once has been sufficiently investigated.

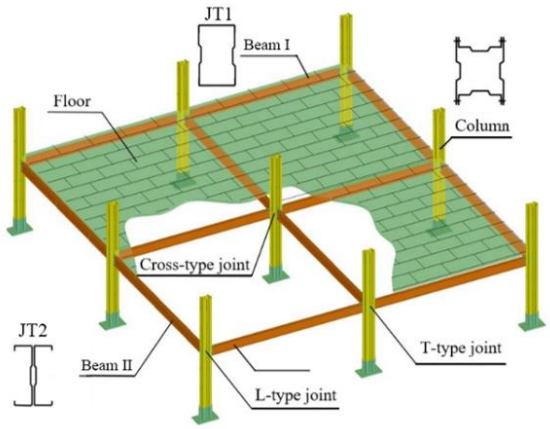


(a) System diagram

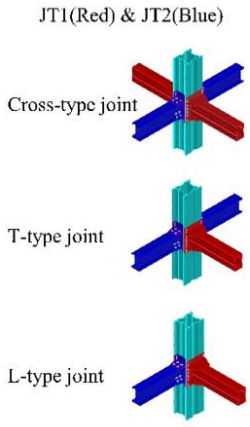


(b) examples of JT1 and JT2 connecting the beams to the columns

Fig. 1. Schematic diagram of the proposed CFS framed structure system: (a) system diagram, and (b) examples of JT1 and JT2 connecting the beams to the columns

The first type of joint (JT1) is an "end plate" beam-to-column joint, as shown in Fig. 2. The joint consists of end plate, stiffening plate, the connected column and the built-up open beam section. The stiffening plate and beam are welded off-site to the end plate of the connection, while the beam with the end plate is connected to the column and cruciform plates by high-strength bolts on-site (Fig.2 (b)).

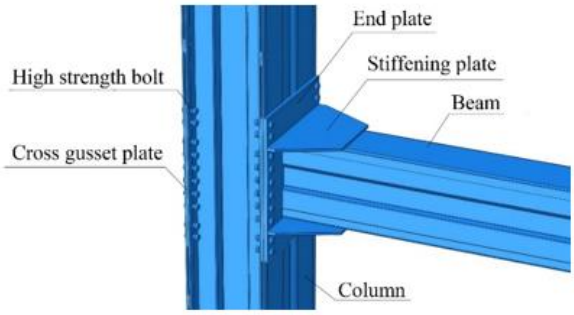


(a) The assembled model of JT1

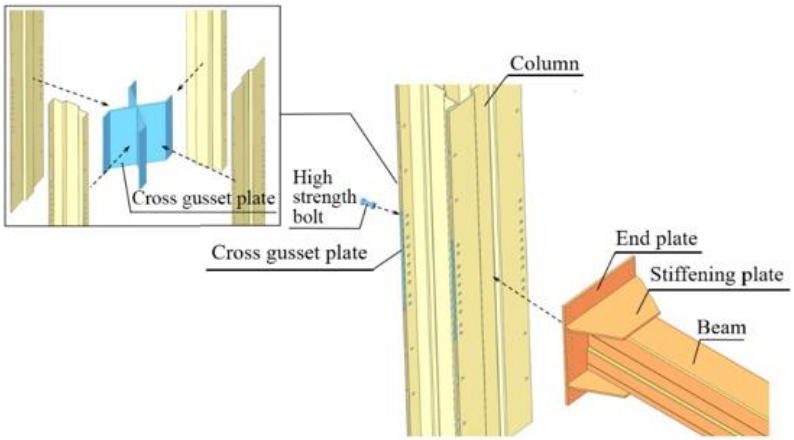


(b) The components of JT1

Fig. 2. Details of JT1: (a) the assembled model, and (b) the components

The second type of joint is the "channel connected" beam-to-column joint, as shown in Fig. 3. The joint consists of channel connectors and the connected column and the built-up close beam section. The steel channel connector is inserted in the concave part of the column edge. The beam and column are connected through the channel connector by high-strength bolts, as shown in Fig.3.

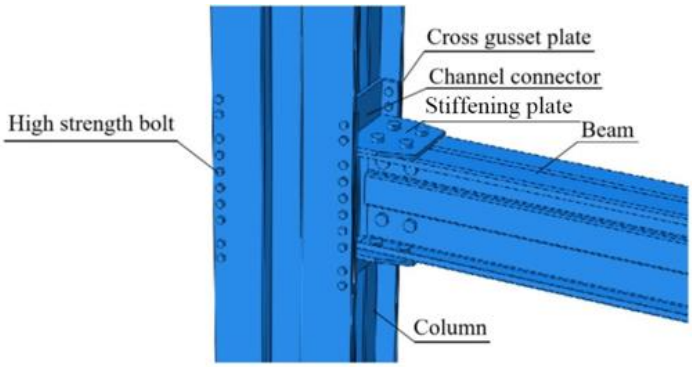


(a) The assembled model of JT2

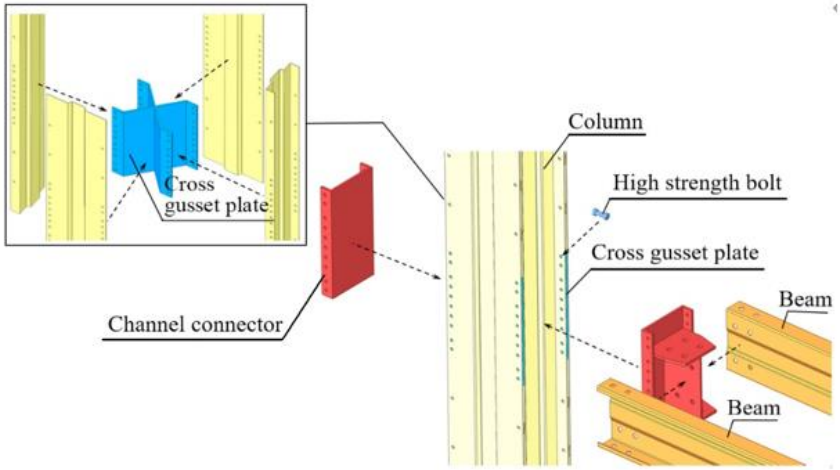


(b) The components of JT2

Fig. 3. Details of JT2: (a) the assembled model, and (b) the components

## 2. Experimental program

### *2.1. Test specimens*

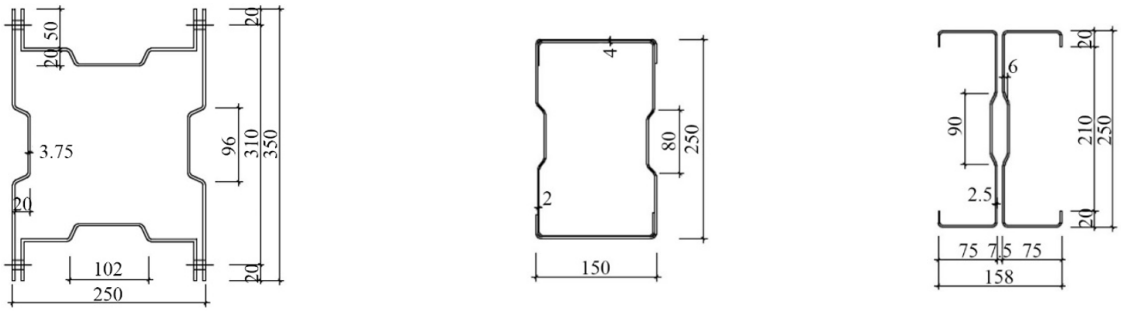


(a) (b) (c)

Fig. 4. Detailed cross-sectional dimensions of the specimens: (a) column; (b) beam I, and (c) beam II (unit in mm)

Full-scale tests of the specimens were carried out under monotonic and cyclic loads. The dimensions of the specimens

were carefully selected from the commonly used cross-sections in industry in China. The detailed column dimensions are shown in Fig. 4 (a). The detailed cross-sectional dimensions of Beam I are shown in Fig. 4 (b), and the detailed cross-sectional dimensions of Beam II are shown in Fig. 4 (c). The column, the beam type II, the gusset plate and the plates of the channel connector are manufactured from Q345B [34] steel with a nominal yield strength of 345 MPa. The type of beam I and end plates are manufactured from Q235B [34] steel with a nominal yield strength of 235 MPa. The high-strength bolts are made of Grade 10.9S material with a nominal yield strength of 900 MPa. Coupon tests were carried out and are reported in detail in Section 2.2. The thickness of the gusset plate, the vertical stiffener in the middle of the channel connector and the stiffening plate are 7.5 mm. The thickness of the end plate, the plates of channel connectors and the vertical stiffeners, are 10 mm.

*2.2. Material properties*

Coupon tests were carried out to measure the material properties of each component in a low speed repeated load tests, according to GB/T 228.1-2010 [35]. Five types of coupons, representing the materials of the columns, beams, gusset plates, channel connectors and end plates, were tested. For each component, three coupons were extracted and tested. Photos of the column and the Beam Ⅱ coupons are shown in Fig. 5. The material stress-strain curves of the Z-2 coupon of the column and the L2-3 coupon of the Beam Ⅱ are shown in Fig. 6 as a typical example. The coupon test results are summarized and shown in Table 1. The coupon test results have been checked against the Chinese standard for seismic design of buildings (GB 50011－2010) [36], and the material properties of the steel used for fabricating the specimens satisfy the requirement of GB 50011－2010. It is worth noting that the cold working effect was not considered when producing the coupons. This is because that according to previous study [37], the effect of cold working on the ultimate moment capacity of the CFS connections is negligible.


(a) (b)

Fig. 5. Photos of the coupons of: (a) the column, and (b) Beam Ⅱ

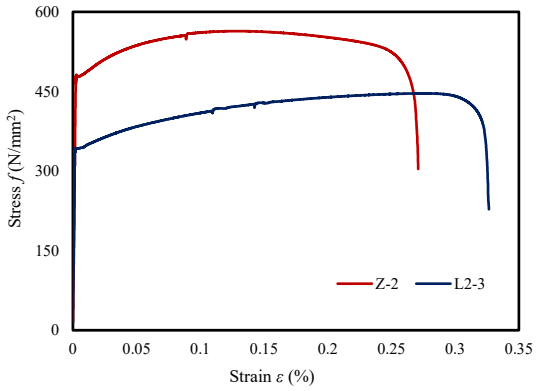


Fig. 6. The tested stress-strain curves of Z-2 of the column and L2-3 of the Beam Ⅱ

Table 1. Material properties (unit: MPa)

| Specimen | Plate number | $f_y$ (MPa) | Mean value | $f_u$ (MPa) | Mean value |
|---|---|---|---|---|---|
| Column | Z-1 | 482.59 | 486.32 | 534.88 | 546.74 |
| | Z-2 | 485.32 | | 550.50 | |
| | Z-3 | 491.05 | | 554.83 | |
| Beam Ⅰ | L-1 | 261.61 | 247.43 | 350.20 | 332.19 |
| | L-2 | 255.25 | | 340.73 | |
| | L-3 | 225.44 | | 305.64 | |
| Beam Ⅱ | L2-1 | 343.21 | 338.50 | 442.78 | 449.70 |
| | L2-2 | 332.48 | | 452.89 | |
| | L2-3 | 339.81 | | 453.44 | |
| Gusset plate | J-1 | 339.48 | 324.30 | 496.19 | 493.37 |
| | J-2 | 338.01 | | 491.26 | |
| | J-3 | 295.41 | | 492.65 | |
| Channel connector | C-1 | 382.65 | 395.56 | 549.28 | 554.91 |
| | C-2 | 412.95 | | 567.17 | |
| | C-3 | 391.08 | | 548.29 | |
| End plate | D-1 | 269.27 | 273.54 | 427.93 | 428.23 |
| | D-2 | 265.76 | | 427.32 | |
| | D-3 | 285.59 | | 429.44 | |

*2.3. Test setup and loading scheme*

The cyclic loading tests of the beam-to-column joints were carried out, on the basis of AISC 341-16 [30] recommendations, in the structural test lab of Ming Palace campus of Nanjing University of Aeronautics and Astronautics. The test setup is shown in Fig. 7. The column was fixed on the flanges of the top and bottom reaction beams with bolts. The height of the column was manufactured to be1600 mm while the overall length of the beam was 1095 mm. The distance between the loading point on the beam and the central axis of the column was 1080 mm. In order to accurately

collect the real-time deformation of the beam-to-column joint, a total of 8 linear variable differential transformers (LVDTs) were set up in each experiment. LVTDs C1 and C2 were vertically installed at the lower flange of the beam close to the column edge to measure the deformation of the beam in the joint area. LVTDs C4 (5) and C6 (7) were horizontally installed on the web surfaces on both sides of the column at the height of the upper and lower ends of the joint area to measure the deformations of the column. LVTDs C8 and C3 were vertically installed at the lower flange of the beam close to the loading point to measure the deformation of the beam end. The installing positions of the LVTDs are shown in Fig. 8 while the detailed dimensions of connections JT1 and JT2 are shown in Fig. 9.

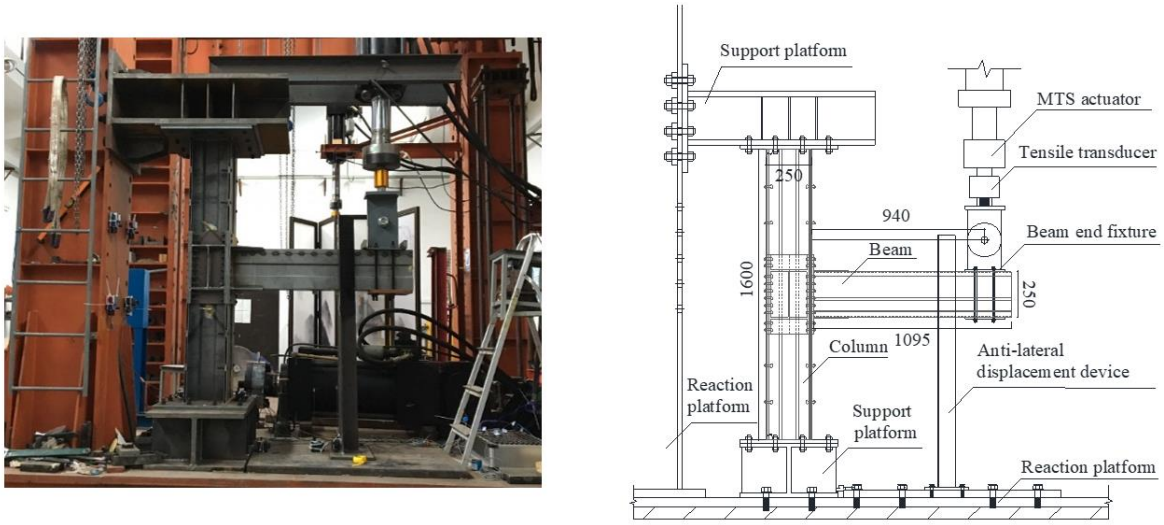


(a) On-site photo (b) Schematic diagram

Fig. 7. Test setup when Beam I is tested: (a) on-site photo, and (b) schematic diagram

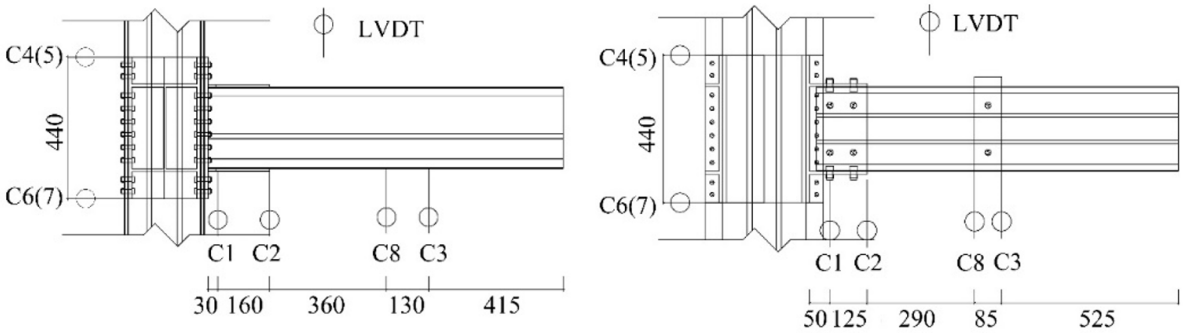


(a) LVTD locations when JT1 was tested (b) LVTD locations when JT2 was tested

Fig. 8. LVTD locations: (a) when JT1 was tested, and (b) when JT2 was tested (unit in mm)

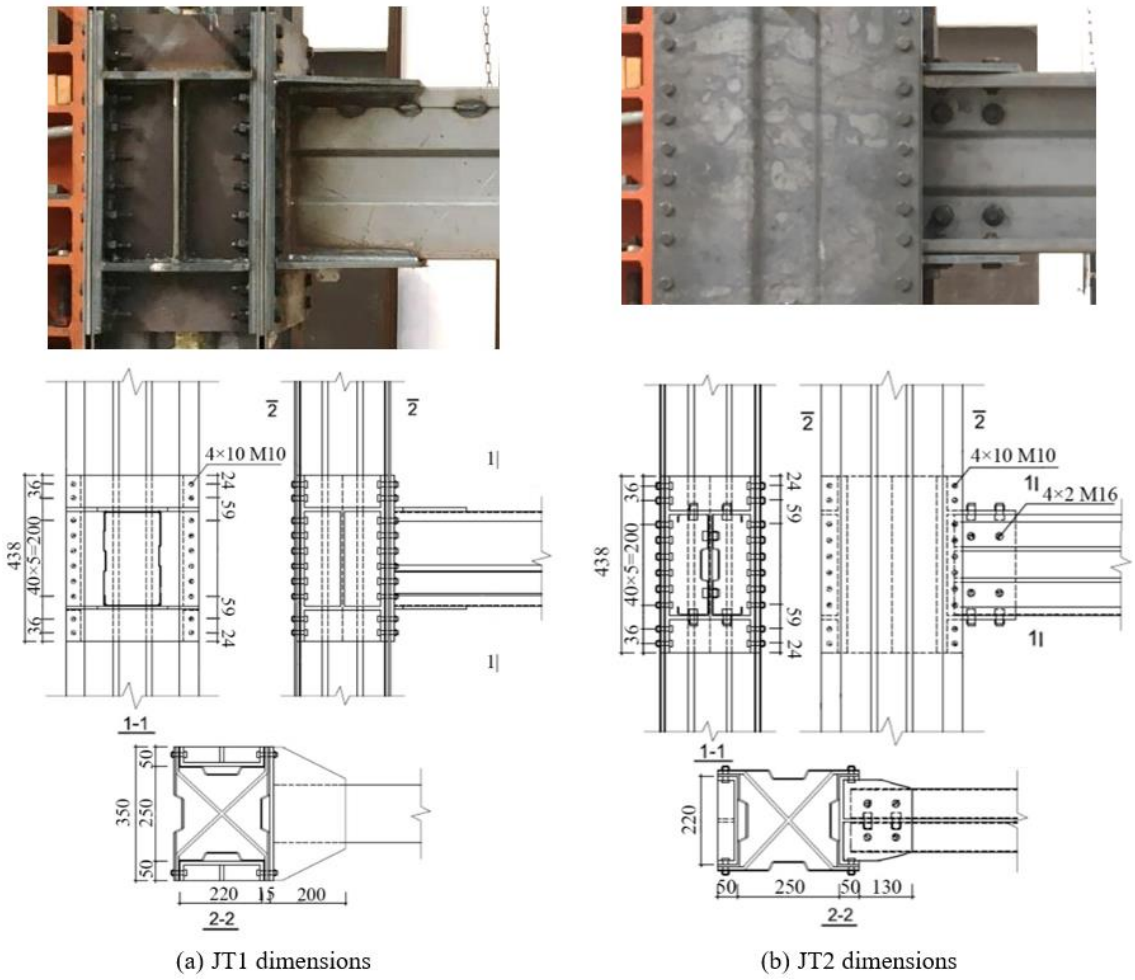


(a) JT1 dimensions (b) JT2 dimensions

Fig. 9. Detailed dimensions of: (a) JT1; and (b) JT2

The cyclic loads were applied to the beam end by a loading actuator in accordance with AISC 341-16 [30] recommendations to classify the beam-column moment connections and to assess whether it belongs to special or intermediate moment frames. The relationship between the designated loading scheme and the load cycle numbers are shown in Fig. 10. The vertical displacement scheme of the actuator was determined by the distance between the loading point and the end of the beam (940 mm) and the inter-story drift angle recommended in AISC 341-05 [38]. Geometric imperfections were not considered in the testing program, as previous research [39] found that the initial imperfection had negligible effect on the cyclic behaviour of the joints when the residual stress and cold work of round corners were ignored at the same time.

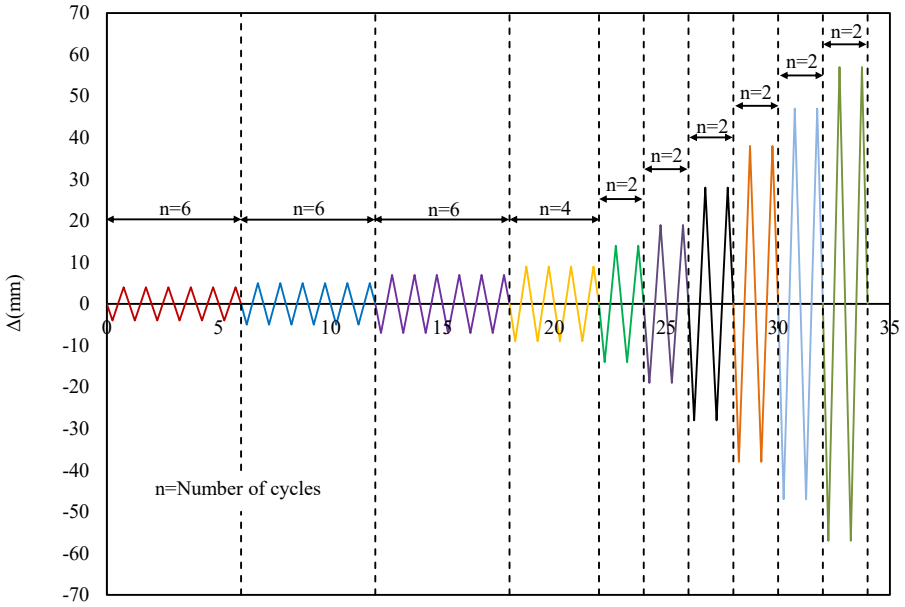


Fig. 10. Cyclic loading protocol.

## 3. Observations in the tests

### *3.1. Overview of the test result*

In order to guarantee the reliability of the results of the low cycle cyclic loading test on the proposed connections, three identical specimens were assembled for each type of beam-to-column connection. The failure modes, ultimate bearing capacity and initial stiffness of JT1 and JT2 are shown in Table 2 and Table 3. It can be seen that the failure modes, stiffness and ultimate capacities of the same type of specimens consistently agreed well with each other in the three tests. The test results and failure modes of each joint will be presented in Section 3.2.

Table 2. Summary of JT1 test results

| Specimen number | JT1-1 | JT1-2 | JT1-3 |
|---|---|---|---|
| Damage pattern |  |  |  |
| Failure mode | The beam flange and web adjacent to the joint area buckled, and cracks appeared on the beam flange | | |
| Maximum moment | 44.46 | 44.89 | 44.74 |
| (kN·m) | -42.90 | -41.59 | -40.96 |
| Initial stiffness | * 6662.90 | 22256.87 | 21768.22 |
| (kN·m/rad) | * 8289.45 | 16633.46 | 17773.21 |

Table 2. Summary of JT1 test results

| Specimen number | JT1-1 | JT1-2 | JT1-3 |
|---|---|---|---|

Note: * represents abnormal data caused by the loosening of displacement meters that were used to measure the parameter.

Table 3. Summary of JT2 test results

| Specimen number | JT2-1 | JT2-2 | JT2-3 |
|---|---|---|---|
| Damage pattern |  |  |  |
| Failure mode | * Two bolts on the upper and lower sides of the column are cut, and the beam is not deformed | The beam flange and web at the edge of the joint area buckled, the beam flange cracked, and the first bolt on the upper side of the column was cut. | |
| Maximum moment (kN·m) | 64.67<br>-64.23 | 68.75<br>-67.62 | 69.87<br>-71.13 |
| Initial stiffness (kN·m/rad) | 6732.56<br>7204.92 | 6425.54<br>8013.89 | 6913.88<br>7181.35 |

Note: * represents the abnormal failure pattern caused by insufficient strength of stud bolt.

### *3.2. Hysteretic behaviour of the tests*

#### *3.2.1. Hysteretic behaviour of JT1*

The moment-rotation ($M$-$\theta_d$) relationship of JT1 subjected to the cyclic loading is presented in Fig. 11. The moment $M$ is the moment produced at the column flange surface and the rotation $\theta_d$ in each cyclic loop is defined in accordance with AISC 341-05 [38], as described in Section 2.3. The key points on the moment-rotation hysteretic curve are: (1) Points A and A$^-$ represent the peak positive and negative bending capacities of the tested joint (44.74 kN·m and -40.96 kN·m) at the corresponding rotations of 0.012 rad and -0.014 rad, respectively. At these points, the beam flanges and the web started to buckle locally at the position that was approximately 30mm away from the edge of the joint area (or about 30 mm away from the first row of bolts in the joint, see in Fig. 11). However, no obvious deformation or failure was observed in the stiffening plates and the end plates. (2) Points B and B$^-$ represent the typical post-failure stage where the beam flanges

and web of the joint area buckled significantly, and cracks appeared on the beam flanges and plastic deformation was also developed at the beams.

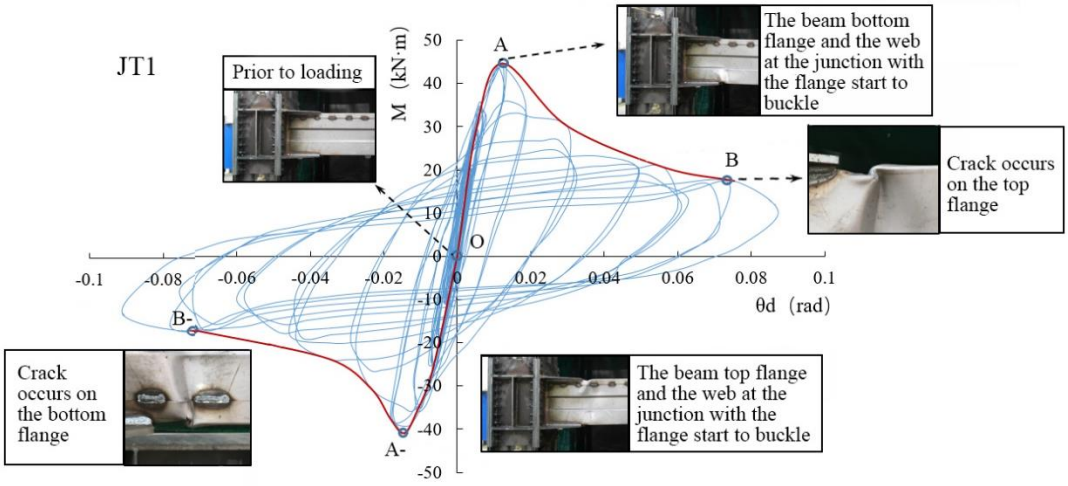


Fig. 11. Experimental phenomena of JT1

The deformation modes in failure of the joint are presented in Fig. 12. At the end of the loading schemes, very slight deformations at the end plate were observed while no obvious deformation was developed in the stiffening plates and the column flange. Before the peak load of the tests (in phases OA and $OA^-$), obvious deformations and movements of the high-strength bolts were observed due to the interaction forces produced at the beam end, the stiffening plate and the end plate, as well as the high-strength bolting between the end plate and the column flange that were under axial forces. In the stages of AB and $AB^-$, the buckling at the beam flanges gradually extended towards the middle of the web. Eventually, the significant plastic residual deformation and fracture occurred in the beam at the vicinity of the cover plates (Fig. 10) and the loading process was terminated.

(a) (b)

Fig. 12. Failure mode of JT1: (a) side view of the buckled web and flanges; and (b) top view of the buckled flanges

*3.2.2. Hysteretic behaviour of JT2*

The moment-rotation ($M$-$\theta_d$) relationships of JT2 under the cyclic loading are presented in Fig. 13. The main information obtained from the moment-rotation hysteretic curves are concluded as (1) The Points A and $A^-$ represent the maximum positive and negative moment capacity of the tested joint (69.87 kN·m and -71.13 kN·m) with the corresponding rotations of 0.045 rad and -0.030 rad. At these points, the buckling of the beam was observed on the beam flanges and the beam web. Different from the joint JT1, relative deformation was observed between the beam flanges and the stiffening plates, which indicated that large deformation at the beam flange developed. The slippage between the beam flanges and the stiffening plates was also observed with bolt hole bearing deformation developed. (2) B and $B^-$ represented the points in a typical post-buckling stage where cracks were observed on the beam flanges adjacent to the stiffening plate edge. Plastic yield line patterns in the beam web also happened between the bottom and top flanges. The corresponding ultimate rotations were 0.112 rad and -0.108 rad, respectively at those points. The failure modes of the joint are shown in Fig. 14. At the initial stages of OA and $OA^-$, when the rotation angle reached ± 0.015 rad, loud noise caused by the slippage among the high-strength bolts and their connected side edges of the channel connector and the column flanges were found. Relative displacements between the channel connector and the column flanges, together with bolt slippage were also observed. The out-of-plane deformation in the column web due to the bending moment transferred from the joint was also detected but no significant plastic yield line patterns were observed in the column web. At the stages of AB and $AB^-$, when the rotation angle increased to ± 0.060 rad, significant yield line patterns started to be observed in the beam flanges and

the beam web but close to the flanges. As the loading continued, the deformation of the beam flanges and the beam web increased gradually. The beam flanges bent outward, and the buckling and plastic deformation of the web close to the beam flanges gradually extended to the middle of the web.

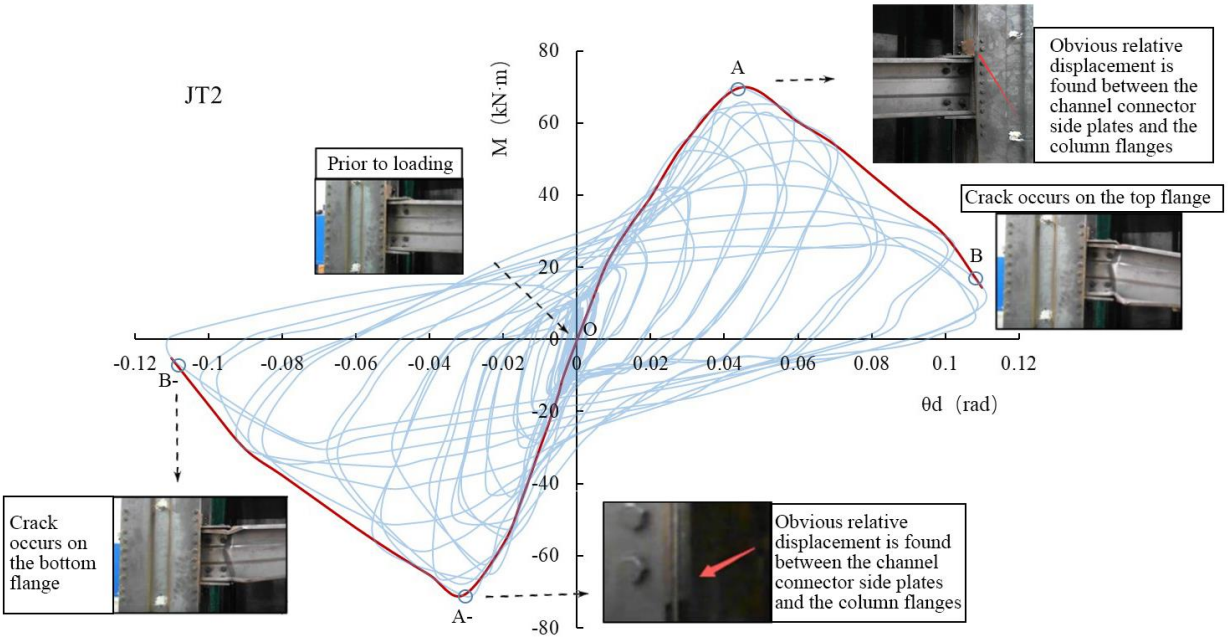


Fig. 13. Experimental phenomena of JT2

(a) side view of the buckled web and flanges

(b) bottom view of the cracked flanges

Fig. 14. Failure mode of JT2: (a) side view of the buckled web and flanges; and (b) bottom view of the cracked flanges

## 4. Analysis of test results

### *4.1. Moment-rotation hysteretic curve*

The moment rotation ($M$-$\theta_d$) hysteresis curve of JT1, which is calculated by deducting the rotation of the column ($\theta_c$) from the overall rotation of the beam-end ($\theta_b$), is shown in Fig. 15 (a). The overall rotation of the beam-end can be calculated according to Eq. (1), and the rotation of the column can be calculated according to Eq. (2).

$$\theta_b = (\delta_3 - \delta_8)/d_b \quad (1)$$

$$\theta_c = [(\delta_4 - \delta_6)/d_c + (\delta_5 - \delta_7)/d_c]/2 \quad (2)$$

where, $\delta_3$ to $\delta_8$ are the displacements measured by the displacement meters at the locations of C3 to C8 shown in Fig. 8.

The hysteresis loop corresponding to the maximum bearing capacity of the joints is shown in Fig. 15 (b). It can be seen that a significant pinch effect is shown in the hysteresis curve of JT1. This reflects that the joint type is less advantageous in absorbing energy, mainly relying on the plasticity in the CFS beam sections. No significant slippage was observed as the bolts in the endplates were under tension. Early local buckling and fracture of the beam end was observed for the JT1 specimen due to the very slender cross-section used in the assembled connection. This causes the immediate stiffness reduction (pinching effect) of cross-sections in the hysteretic curves. The rotation angle of the column, which is calculated according to the horizontal displacements measured by LVTDs C4, C5, C6 and C7, is shown in Fig. 15 (c). It can be seen that the measured column rotation is small compared with the overall rotation of the beam end. The rotation angle of the joint, which is calculated according to the horizontal displacements measured by LVTDs C1 and C2, is shown in Fig. 15 (d). This rotation angle was mainly caused by the bolt shank elongation which resulted in the rigid inclination of the beam end. This rotation also contributed to a negligible portion of the overall beam-end rotation of JT1.

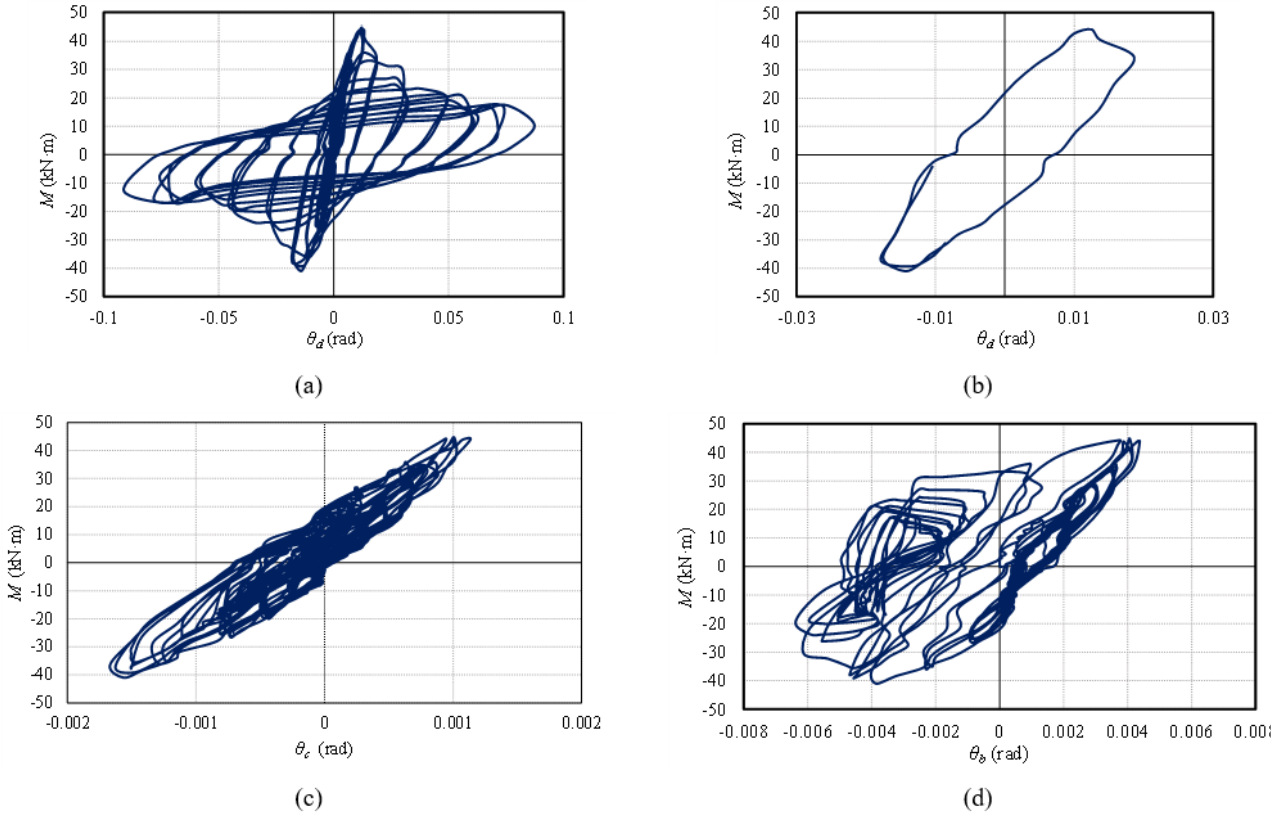


Fig. 15. Moment rotation hysteretic curve of JT1: (a) joint hysteresis curve; (b) hysteresis loop under maximum bearing capacity ($\theta_d$ = 0.012rad); (c) rotation angle of column axis $\theta_c$, and (d) rotation angle at the end plate $\theta_b$;

The moment rotation ($M$-$\theta_d$) hysteresis curve of JT2 is shown in Fig. 16 (a). The curve is calculated according to the same method as that of JT1. The hysteresis loop corresponding to the maximum bearing capacity of the joints is shown in Fig. 16 (b). Pinch effect can be observed in the hysteresis curve of JT2, which was caused by the bolt slippage that occurred at the connecting edges between the channel connector and the column flanges. The rotation angle of the column, which is calculated according to the horizontal displacements measured by LVTDs C4, C5, C6 and C7, is shown in Fig. 16 (c). It can be seen that the measured column rotation is negligible compared with the overall rotation of the beam end. It is worth noting that the column rotation shown in Fig. 16 (c) could not reflect the column web elastic deformation caused by the bending moment transferred from the joint, as the LVTDs C4, C5, C6 and C7 were placed on the opposite side of the column. The rotation angle of the channel connector, which is calculated according to the horizontal displacements measured by LVTDs C1 and C2, is shown in Fig. 16 (d). This rotation angle was caused by the rotation of the column web, bolt slippage at the interface of the channel connector side plates, as well as the stiffening plates inclination. It can be seen that the joint rotation contributed to a contribute to a significant portion of the overall beam-end rotation of JT2.

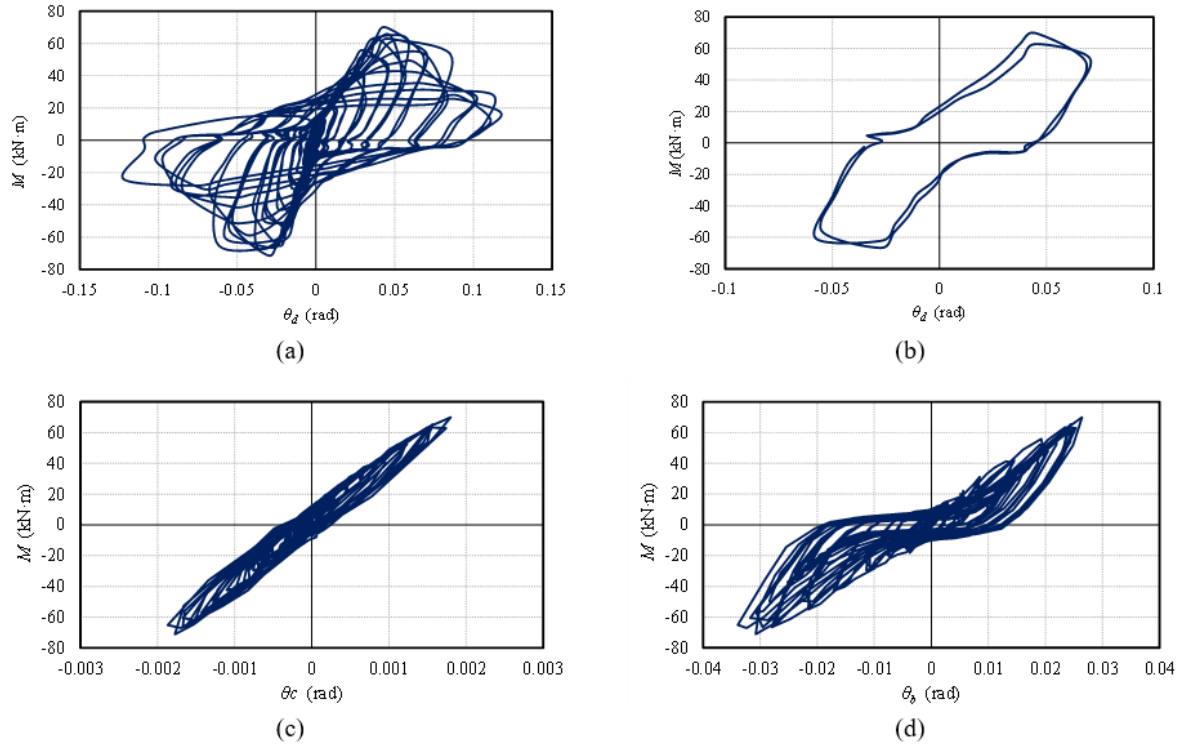


Fig. 16. Moment-rotation hysteretic curve of JT2: (a) joint hysteresis curve, and (b) hysteresis loop under ultimate bearing capacity ($\theta_d$ =0.045rad); (c) rotation angle of column axis $\theta_c$, and (d) rotation angle at the channel connector $\theta_b$

*4.2. Strength and ductility*

The summary of the load-bearing capacities and rotations of the beam-to-column joints under low cyclic loading is shown in Table 4. It can be seen that due to the differences in material and cross-section types between the two joints, the bearing capacity of JT2 is greater than that of JT1. The nominal moment capacity ($M/M_p$) of JT1 is smaller than 1.0, and the nominal moment capacity of JT2 is larger than 1.0, which indicate that the joint JT2 performs better than JT1 in terms of increased maximum flexural capacity, therefore can effectively delay the local buckling at the end of the beam.

Table 4. Summary of low cycle repeated load test results

| Joint number | Maximum bending moment (kN·m) | Ultimate angle $\theta_u$ (rad) | Termination angle $\theta_d$ (rad) |
|---|---|---|---|
| JT1 | 40.96 | 0.023 | 0.070 |
| JT2 | 69.87 | 0.066 | 0.108 |

The backbone curves of normalized moment $M/M_p$ against joint rotation $\theta_d$ of JT1 and JT2 in the cyclic loading tests are shown in Fig. 17, where $M_p$ is the plastic flexural strength of the beam sections. $M_p$ equals to 57.4 kN·m for Beam Ⅰ and 63.6 kN·m for Beam Ⅱ.

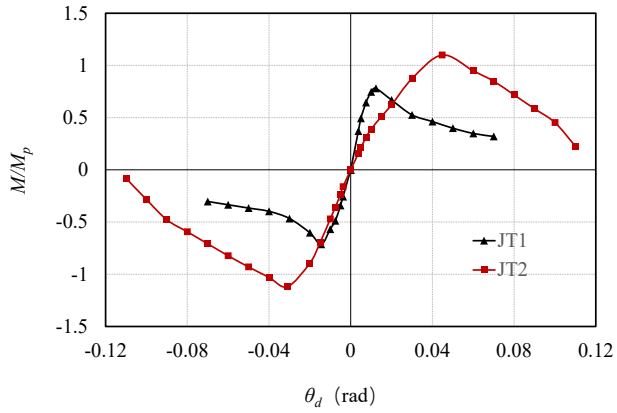


Fig. 17. Normalized moment rotation backbone curves of JT1 and JT2

Ductility is defined as the structural ability to resist plastic deformations without significant loss of strength. According to seismic design guidelines [40], connection ductility is an important index to evaluate the mechanical properties of the structure to resist high seismic loads. Ductility ratio ($\mu$) is defined as the ratio of the ultimate rotation ($\theta_u$) to the yield rotation ($\theta_y$), calculated by

$$\mu = \frac{\theta_u}{\theta_y} \tag{3}$$

The yield rotation $\theta_y$ is calculated according to the FEMA bilinear idealization model [41]. In the FEMA idealized bilinear curve, $\theta_y$ is calculated based on the condition that the secant slope intersects the actual envelope curve at 60% of the nominal yield flexure capacity ($M_y$), and the area under the bilinear curve is set to be equal to that enclosed by the original curve up to the target rotation $\theta_t$ (see Fig. 18). In this research, $\theta_y$ is calculated based on the condition that the secant slope intersects the actual envelope curve at 60% of the nominal yield moment ($M_y$), while the area under the bilinear curve is set to be equal to that enclosed by the original curve up to the target rotation ($\theta_t$). In this research, the target rotation $\theta_t$ is set to be $\theta_u$, which is the joint rotation at which the joint flexural capacity of the joint equals 80% of its ultimate capacity. The ductility ratio $\mu$ of the two joints calculated by the method mentioned above are shown in Table 5. It can be seen that the ductility ratio of JT2 is larger than that of JT1, which indicates that JT2 possesses a higher ability to undergo plastic deformations without significant loss of strength than JT1.

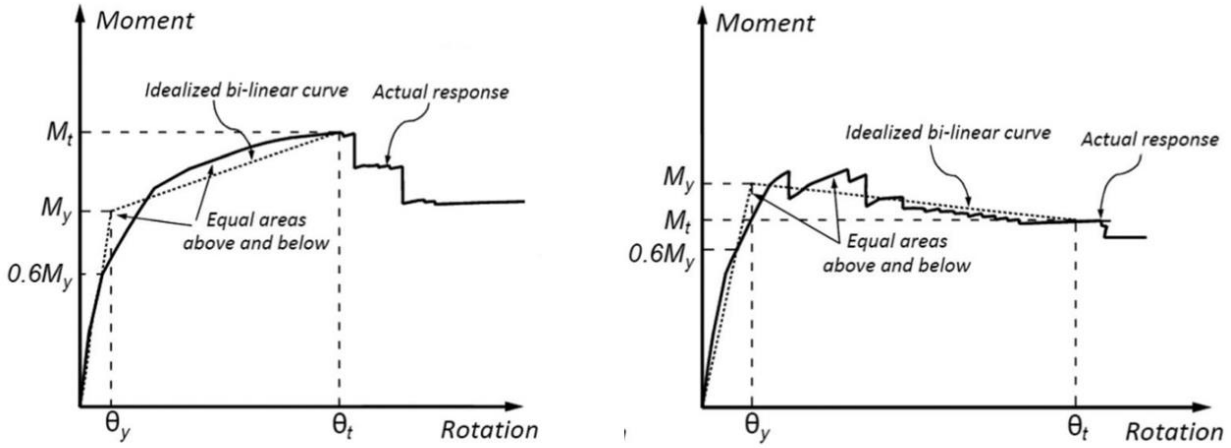


Fig. 18. FEMA bi-linear idealization model: (a) Positive post-yield slope, (b) Negative post-yield slope [41]

Table 5. Ductility coefficient $\mu$ of the two joints

| Joint number | $\theta_y$ (rad) | $\theta_u$ (rad) | $\mu$ |
|---|---|---|---|
| JT1 | 0.00942 | 0.02235 | 2.37 |
| JT2 | 0.01800 | 0.06690 | 3.72 |

Apart from the ductility ratio to evaluate the joint ductility under seismic load, current seismic design guidelines (e.g. AISC 341-16 [30] and Eurocode 8 [40]) classify steel moment frame system into Special Moment Frames (SMFs), Intermediate Moment Frames (IMFs), and Ordinary Moment Frames (OMFs) based on their ductility. AISC 341-16 [30] suggests that connections used in SMFs should be capable of exhibiting over 0.04 radians of inter-storey drift while sustaining 80% of the beam section plastic moment resistance; connections used in IMFs are expected to withstand the inter-storey drift of between 0.02 and 0.04 rad while sustaining 80% of the beam section plastic moment resistance, and no rotational ability requirement is introduced to connections used in OMFs. In the absence of clear criteria for CFS frame systems, the same definitions are used in this study to assess the ductility CFS connections for seismic applications. It can be evaluated from Fig. 17 that the moment capacity of JT1 is not able to reach $0.8M_p$. The inter-storey drift of JT2 is 0.071 rad when the rotational strength descends to $0.8M_p$. Therefore, JT1 satisfies the OMFs requirements and JT2 satisfies the SMFs requirements in terms of the rotation capacity and the strength-degrading regime.

*4.3. Joint rigidity and stiffness degradation*

The joint initial stiffness is another indicator to evaluate the joint rotation behaviour. The initial stiffness values of JT1 and JT2 are 17773.21 kN·m/rad and 6913.88 kN·m/rad, respectively**Error! Reference source not found.**. The connection structure is symmetrical, but due to the installing imperfect positioning and buckled deformation of the beams, the forward and reverse initial stiffnesses of each node are not completely identical. However, the differences between

the measured positive and negative initial stiffness values of both the joints are within an acceptable range, and the joint initial stiffnesses are obtained by taking the minimum absolute value of the positive and negative initial stiffness values.

According to Eurocode 3 Part 1-8 [42], when the initial stiffness $S_{j,ini}$ of the joint is smaller than the value of $0.5L_b/EI_b$, the joint is classified as simple joint. Whereas when $S_{j,ini}$ is larger than the value of $25L_b/EI_b$, the joint is classified as rigid joint. The joint initial stiffness can be calculated according to Eq. (4):

$$S_{j,ini} = K_b L_b / EI_b \tag{4}$$

where $L_b$ and $EI_b$ are the length and bending rigidity of the beam, respectively.

It is worth noting that the approach recommended in Eurocode 3 Part 1-8 [42] is adopted to classify the connection stiffness. Therefore, the rotation caused by the out-of-plane column flange deformation is not included in the calculation and evaluation of joint rigidity. The $M/(\theta_b-\theta_c)$ curves of JT1 and JT2 are shown in Fig. 19 and Fig. 20, respectively. $M$ is the bending moment at the column face and the relative beam-column rotations $(\theta_b-\theta_c)$ are taken as the difference of the values measured by displacement meter 1, 2, 4, 5, 6 and 7, as shown in Fig. 8. The red lines are the initial stiffnesses of the joints. The blue dotted lines represent the boundary stiffness of rigid joints and the green dotted lines represent the boundary stiffnesses of the simple joints. It can be seen that the initial stiffnesses of both JT1 and JT2 lie between the lines representing the boundaries of rigid joint and simple joint, and therefore JT1 and JT2 can be classified as semi-rigid joints. JT1 exhibits higher stiffness than JT2.

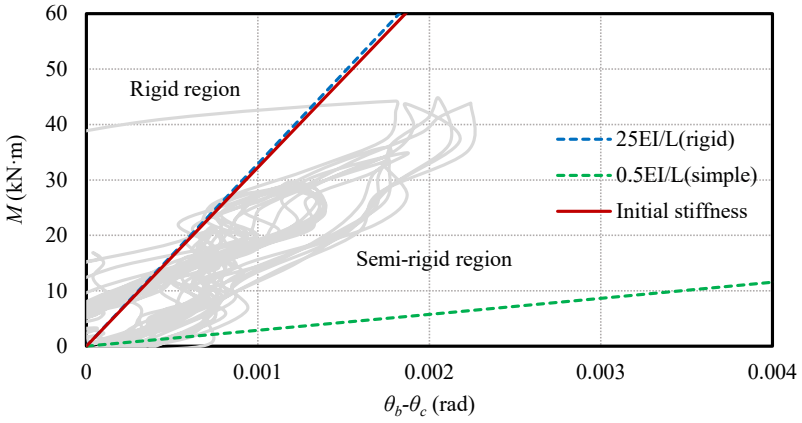


Fig. 19. The initial stiffness of JT1

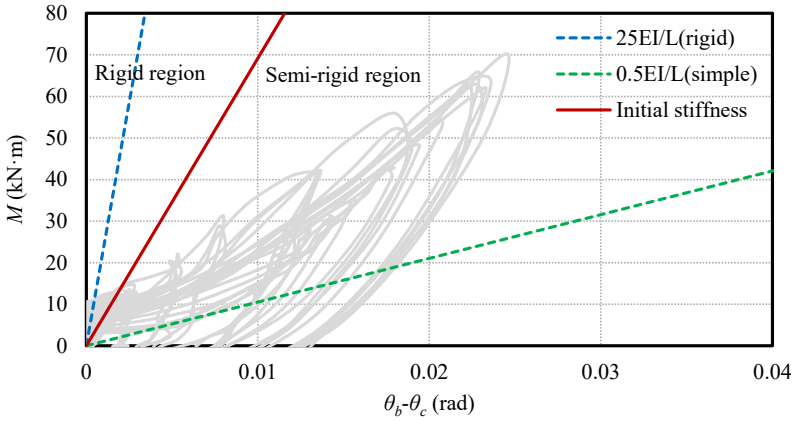


Fig. 20. The initial stiffness of JT2

The joint stiffness-rotation degradation curves are shown in Fig. 21. The joint stiffness $K$ and the rotation in each cyclic loop $\theta$ are normalized by dividing the initial secant stiffness and the ultimate rotation $\theta_u$, respectively. The joint stiffness $K$ of each loop is approximately obtained by taking a tangent segment from the original point in the corresponding loop. In Fig. 21, the black solid lines represent the normalized stiffness-rotation relationship of JT1, and the red dashed lines represent the normalized stiffness-rotation relationship of JT2. The stiffness degradation values are shown up to the ultimate rotation of the joints with $\theta/\theta_u$ equals to 1. It can be seen that due to the symmetry of the joints, the stiffness degradation trend of each joint is similar with an acceptable variation between the positive and negative loading processes. With the increase of storey drift angle, the stiffness degradation of JT1 started to accelerate when the beam-end rotation $\theta$ equals 0.3 $\theta_u$ approximately, at which point the buckling at the end of the beam starts. In comparison, the stiffness degradation of JT2 started to accelerate at a lower storey drift of approximately $0.1\theta_u$. For the negative loading process, the accelerating point is when the storey drift angle equals to approximately $0.5\theta_u$ where the buckling at beam ends initiates. Overall, the stiffness of JT1 is larger than that of JT2, and the stiffness degradation of JT2 is faster than that of JT1.

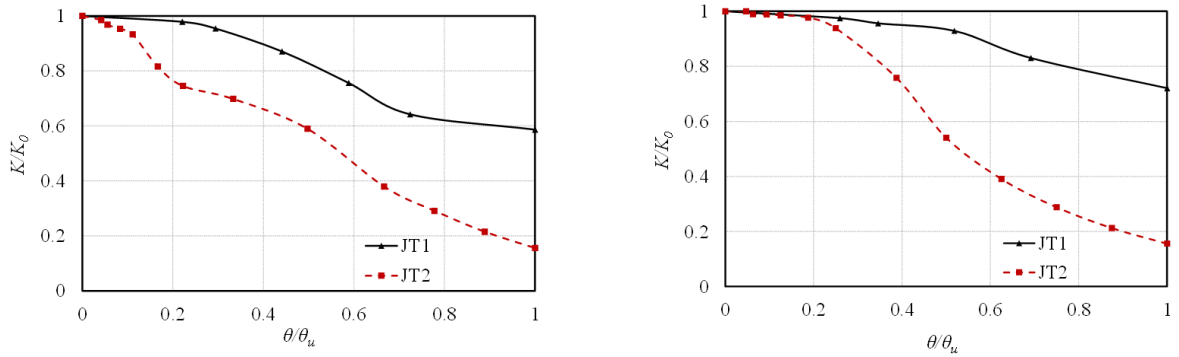


Fig. 21. Stiffness degradation: (a) Stiffness degradation of the joints subject to positive loading;(b) Stiffness degradation of the joints subject to negative loading

From the curve in Fig. 21, it can also be seen that: In the middle and later stage of the loading process, the stiffness degradation speed of JT2 is lower than JT1. In the early loading process, the stiffness degradation of JT2 was mainly caused by the relative displacement of plates and deformations between the channel connector and the column flange. However, in the later stage, the plastic deformation of the beam member at the edge of the joint area started to happen, and no significant plastic deformation in the channel connector and the column flange was observed therefore the joint stiffness degradation of JT2 is less substantial.

*4.4. Equivalent viscous damping coefficient*

Equivalent viscous damping coefficient $h_e$ is an important parameter to evaluate the energy dissipation capacity of structures [43]. This coefficient is equal to the ratio of the energy dissipated by the structure in one specific hysteresis cycle over the energy dissipated by its equivalent elastic counterpart when the same deformation is achieved. The structure energy dissipation capacity normally increases with the increase of $h_e$. The equivalent viscous damping coefficient $h_e$ can be calculated by the formula (8) in a single hysteresis loop [44]:

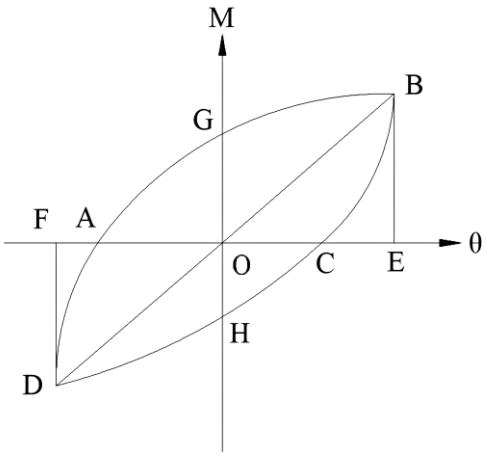

Fig. 22. Calculation of equivalent viscous damping coefficient $h_e$

$$h_e = \frac{1}{2\pi} \cdot \frac{S_{ABCD}}{S_{\Delta OBE} + S_{\Delta ODF}} \tag{5}$$

where, $S_{ABCD}$ is the envelope area of the hysteresis loop to represent the energy dissipated under one cycle of loading. $S_{\triangle OBE}$ and $S_{\triangle ODF}$ are the areas of triangle OBE and triangle ODF, respectively, to represent the energy dissipated to be subjected to the same positive and negative displacements when the joint is assumed to be elastic.

The values of the equivalent viscous damping coefficient $h_e$ calculated under each loading cycle are shown in Fig. 23. It can be seen that the equivalent viscous damping coefficients of JT1 and JT2 show an increasing trend, which indicates that the joint energy dissipation capacities gradually increase with the development of plastic deformation. It is also shown that the $h_e$ of JT2 increases slower than that of JT1, possibly because that JT2 had a higher moment resisting capacity than JT1. For the same applied end displacement of the beam, the plastic deformation developed in JT2 is less than that developed in JT1. However, the final viscous damping coefficient of JT2 is larger than JT1, which indicates that JT2 has better plastic deformation and energy dissipation capacity than JT1.

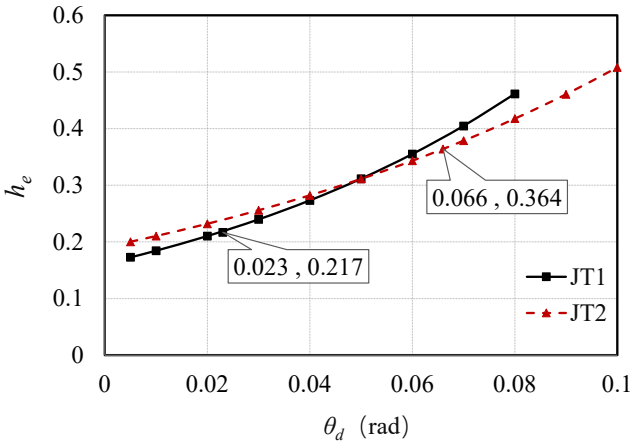


Fig. 23. Equivalent viscous damping coefficients JT1 and JT2 calculated under each loading cycle

The coefficient $h_e$ under two cases are particularly evaluated in this research: (1) loop with peak bending capacity, when the joints reached their maximum bending capacity; and (2) loop corresponding to 80% of ultimate flexural capacity. The equivalent viscous damping coefficient $h_e$ of the two cases is shown in Table 6. It can be seen that the equivalent viscous damping coefficients at the loop of 80% ultimate capacity are larger than those at the loop of peak capacity for both joints. This indicates that as energy dissipation mainly relied on plastic deformation, when the joints were loaded to the 80% of ultimate moment loop, plastic deformations were more significant than those when the joints were at the peak capacity loop. The equivalent viscous damping coefficients of JT2 are larger than those of JT1, which indicates that JT2

had better energy dissipation capacity than JT1 at both the peak capacity loop and the 80%ultimate capacity loop.

Table 6. Equivalent viscous damping coefficients of the tested joints

| Joint number | JT1 | JT2 |
|---|---|---|
| peak capacity loop | 0.190 | 0.296 |
| 80% ultimate capacity loop | 0.219 | 0.367 |

*4.5. Energy dissipation capacity*

The envelope areas of the hysteretic loops (shown in Fig. 15 (a) and Fig. 16 (a)) reflect the energy dissipation of the joints subjected to the cyclic loading scheme. The cumulative energy dissipations at each rotation angle at the beam end of JT1 and JT2 are shown in Fig. 24. It is worth noting that there were multiple loops at each loading cycle, therefore, the cumulative energy consumptions at each rotation angle were calculated by adding up the areas of all the moment-rotation hysteretic curves at the calculated loading cycle and those of the loading cycles. The area of each moment-rotation hysteretic curve was calculated by an integration programme in Matlab.

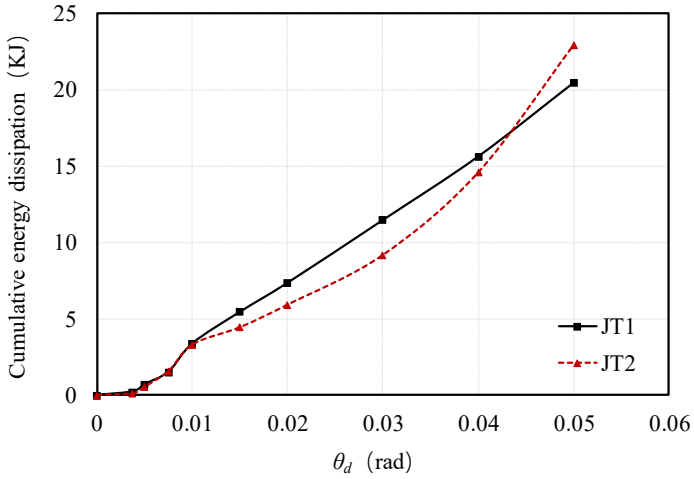


Fig. 24. Comparison of cumulative energy consumption of JT1 and JT2

It can be seen that the cumulative energy dissipations of both joints increase with the increase of the applied displacement at the end of the beam. The cumulative energy dissipation of JT1 is larger than that of JT2 when the inter-storey drift is smaller than 0.45 rad, and smaller than that of JT2 when the inter-storey drift is larger than 0.45 rad. This indicates that JT2 has a better energy dissipation ability that of JT1 at the later stage of the loading scheme.

## 5. Conclusions

An experimental study on two types of new CFS moment-resisting joints was presented in this paper. The two types of joints were designed aiming at postponing the local buckling phenomenon of the connected beams, therefore improving

the joints' rotational capacity and energy dissipation capacities under cyclic load. Through the tested results, the joints were evaluated based on the indicators of strength, ductility, stiffness, equivalent viscous damping coefficient and energy dissipation capacity. From the test programme, the following conclusions can be drawn:

(1) The behaviour of the joints in the tests shows that the Joint Type 1 (JT1) possesses a rigid connection zone which shows negligible deformation during the loading process. The beam flange and web local buckling adjacent to the connection zone produced the degradation of stiffness and strength JT1. Pinch effect was observed in the moment-rotation hysteretic curve of both joints, which was mainly caused by the friction and beam flange and web local buckling adjacent to the connection zone. The nominalized ultimate bending capacity ($M/M_p$) of JT1 is smaller 1, while the ultimate capacity of JT2 is larger than 1. The beams buckled before obvious damage of the tested joints. The tested two types of joints satisfy the seismic design philosophy of 'strong connection-weak beam'.

(2) The strength of JT2 is higher than that of JT1. JT2 obtains a better structural ability to resist plastic deformations without significant loss of strength; this was evaluated by ductility ratio. The rotational capacity of JT1 is not able to reach 0.8 times of the beam plastic moment capacity ($M_p$). Therefore, JT1 fulfilled the requirements of Ordinary Moment Frames (OMFs) defined in AISC Seismic Provisions [38]. The rotational capacity of JT2 is larger than 0.04 rad when the flexure resistance is not smaller than $0.8M_p$, which satisfied the requirements of Special Moment Frames (SMFs) defined in AISC Seismic Provisions [38].

(3) The connections of both JT1 and JT2 can be classified as semi-rigid connections based on their stiffness in all the loops in the moment-rotation hysteretic curves, according to the approach recommended by Eurocode 3 Part 1-8 [42]. The JT1 obtains higher stiffness than JT2. However, JT2 provides better energy dissipation capacity than that of JT1, measured by the equivalent viscous damping coefficient and the envelope areas of the hysteretic loops.

(4) Overall, JT2 exhibits higher performance in terms of strength, ductility, and energy dissipation capacity at later stage of the loading scheme than JT1 for CFS framed building structures to be potentially used in seismic regions.

The proposed two types of joints offer moderate performances to resist the applied cyclic load. Despite that the two tested joint types can provide reasonably good strength to enable that the beam local buckling of the joints is postponed, the joints plastic performance and ductility need to be improved with a better balance in terms of joint strength and the connected member slenderness. In future work, a thorough numerical analysis will be carried out to investigate the

possible methods to improve the joint plastic performance and ductility. Potential key parameters to be considered include the stiffening plate thickness, beam cross-sectional dimensions, and bolt distance, etc. Design procedures and formulas are to be proposed to standardize the joint design, while maximizing the utilization of all the structural components in the joints.

**Acknowledgments**

The reported research work was sponsored by the general program of Jiangsu Natural Science Foundation (BK20191268) and technology development fund for local regions from central government (XZ202201YD0032C).

**References**

[1] Peterman, K. D., Nakata, N., & Schafer, B. W. Hysteretic characterization of cold-formed steel stud-to-sheathing connections, Journal of Constructional Steel Research. 101 (2014) 254-264. https://doi.org/10.1016/j.jcsr.2014.05.019.

[2] Madsen, R. L., Castle, T. A., & Schafer, B. W. (2016). Seismic Design of Cold-Formed Steel Lateral Load-Resisting Systems. NEHRP Seismic Design Technical Brief, 12.

[3] Pham, C. H., & Hancock, G. J. Direct strength design of cold-formed purlins, Journal of structural engineering. 135 (2009) 229-238.

[4] Pham, C. H., & Hancock, G. J. Numerical simulation of high strength cold-formed purlins in combined bending and shear, Journal of Constructional Steel Research. 66 (2010) 1205-1217. https://doi.org/10.1016/j.jcsr.2010.04.014.

[5] Rasmussen, K. J. R., & Gilbert, B. P. Analysis-based design provisions for steel storage racks, Journal of Structural Engineering. 139 (2013) 849-859. https://doi.org/10.1061/(ASCE)ST.1943-541X.0000665.

[6] Zhao, X., Dai, L., & Rasmussen, K. J. Hysteretic behaviour of steel storage rack beam-to-upright boltless connections, Journal of Constructional Steel Research. 144 (2018) 81-105. https://doi.org/10.1016/j.jcsr.2018.01.006.

[7] Hadjipantelis, N., Gardner, L., & Wadee, M. A. Prestressed cold-formed steel beams: Concept and mechanical behaviour, Engineering Structures. 172 (2018) 1057-1072. https://doi.org/10.1016/j.engstruct.2018.06.027.

[8] Lim, J. B., & Nethercot, D. A. Stiffness prediction for bolted moment-connections between cold-formed steel members, Journal of constructional steel research. 60 (2004) 85-107. https://doi.org/10.1016/S0143-974X(03)00105-6.

[9] Lim, J. B., & Young, B. Effects of elevated temperatures on bolted moment-connections between cold-formed steel

members, Engineering structures. 29 (2007) 2419-2427. https://doi.org/10.1016/j.engstruct.2006.11.027.

[10] Rinchen. R, Rasmussen, K. J. Numerical modelling of cold-formed steel single C-section portal frames, Journal of Constructional Steel Research. 158 (2019) 143-155. https://doi.org/10.1016/j.jcsr.2019.03.024.

[11] J.B.P. Lim, D.A. Nethercot. Finite element idealization of a cold-formed steel portal frame, J. Struct. Eng. 130 (2004) 78–94. https://doi.org/10.1061/(ASCE)0733-9445(2004)130:1(78).

[12] Fiorino, O. Iuorio, R. Landolfo. Designing CFS structures: the new school bfs in Naples, Thin-Walled Struct. 78 (2014) 37-47. https://doi.org/10.1016/j.tws.2013.12.008.

[13] J.B.P. Lim, D.A, Nethercot. Ultimate strength of bolted moment-connections between cold-formed steel members, Thin-Walled Struct. 41 (2003) 1019-1039. https://doi.org/10.1016/j.tws.2013.12.008.

[14] Sabbagh A B. Experimental work on cold-formed steel elements for earthquake resilient moment frame buildings, Engineering Structures. 42 (2012) 371-386. https://doi.org/10.1016/j.engstruct.2012.04.025.

[15] Kyvelou, P., Kyprianou, C., Gardner, L., & Nethercot, D. A. (2019). Challenges and solutions associated with the simulation and design of cold-formed steel structural systems. Thin-Walled Structures, 141, 526-539. https://doi.org/10.1016/j.tws.2019.04.030.

[16] Chung KF, Lau L, Experimental investigation on bolted moment connections among cold formed steel members, Engineering Structures. 21 (1999) 898–911. https://doi.org/10.1016/S0141-0296(98)00043-1.

[17] Sabbagh, A. B., Petkovski, M., Pilakoutas, K., & Mirghaderi, R., Ductile moment-resisting frames using cold-formed steel sections: An analytical investigation, Journal of constructional steel research. 67 (2011) 634-646.

[18] AISI S100, North American specification for the design of cold-formed steel structural members, Washington (DC): American Iron and Steel Institute; 2007.

[19] Eurocode 3: design of steel structures: part 1.3: general rules-supplementary rules for cold formed thin gauge members and sheeting. ENV 1193-1-3; 1996.

[20] Uang, C. M., Sato, A., Hong, J. K., & Wood, K., Cyclic testing and modelling of cold-formed steel special bolted moment frame connections, Journal of Structural Engineering. 136 (2010) 953-960. https://doi.org/10.1061/(ASCE)ST.1943-541X.0000190.

[21] Phan, DT, Mojtabaei, SM, Hajirasouliha, I, Lau, TL, Lim, JBP, Design and Optimization of Cold-Formed Steel Sections in Bolted Moment Connections Considering Bimoment, Journal of Structural Engineering. 146 (2020). https://doi.org/10.1061/(ASCE)ST.1943-541X.0002715.

[22] Eurocode 3: Design of steel structures, Part 1–5: Plated structural elements. Brussels: CEN;2006.

[23] Papargyriou, I., Mojtabaei, S. M., Hajirasouliha, I., Becque, J., & Pilakoutas, K., Cold-formed steel beam-to-column bolted connections for seismic applications, Thin-Walled Structures 172 (2022): 108876. https://doi.org/10.1016/j.tws.2021.108876.

[24] Mojtabaei, SM, Becque, J, Hajirasouliha, I, Local Buckling in Cold-Formed Steel Moment-Resisting Bolted Connections: Behavior, Capacity, and Design, Journal of Structural Engineering. 146 (2020). https://doi.org/10.1061/(ASCE)ST.1943-541X.0002730.

[25] Lee, YH, Tan, CS, Tahir, MM, Mohammad, S, Shek, PN, Lee, YL, Influence of Angle Thickness towards Stiffness and Strength Prediction for Cold-Formed Steel Top-Seat Flange Cleat Connection, Applied Science and Precision Engineering Innovation. (2014): 479-480 . https://doi.org/10.4028/www.scientific.net/AMM.479-480.1144.

[26] Siang, TC, Tahir, MM, Ngian, SP, Kueh, A, Experimental Investigation on Slip-in Connection for Cold-formed Steel Double Channel Sections, Advanced building materials. (2011) 1038-1041. https://doi.org/10.4028/www.scientific.net/AMR.250-253.1038.

[27] Ye, J., Mojtabaei, S. M., Hajirasouliha, I., & Pilakoutas, K., Efficient design of cold-formed steel bolted-moment connections for earthquake resistant frames, Thin-Walled Structures. 150 (2020). https://doi.org/10.1016/j.tws.2018.12.015.

[28] Ye J, Mojtabaei S M, Hajirasouliha I, Seismic performance of cold-formed steel bolted moment connections with bolting friction-slip mechanism, Journal of Constructional Steel Research. 156 (2019) 122-136. https://doi.org/10.1016/j.jcsr.2019.01.013.

[29] A. Sato, C.-M. Uang Seismic design procedure development for cold-formed steel–special bolted moment frames. Journal of Constructional Steel Research, 65 (4) (2009): 860-868.

[30] ANSI/AISC, 341-16, Seismic Provisions for Structural Steel Buildings, American Institute of Steel Construction (AISC), 2016.

[31] Jun, et al. An improved and robust finite element model for simulation of thin-walled steel bolted connections. Engineering Structures 250 (2022). https://doi.org/10.1016/J.ENGSTRUCT.2021.113368.

[32] X. Yun, L. Gardner, Numerical modelling and design of hot-rolled and cold-formed steel continuous beams with tubular cross-sections, Thin-Walled Struct. 132 (2018) 574-584. https://doi.org/10.1016/j.tws.2018.08.012.

[33] B.W. Schafer, Z. Li, C.D. Moen, Computational modelling of cold-formed steel, Thin-Walled Struct. 48 (2010) 752-

762. https://doi.org/10.1016/j.tws.2010.04.008.

[34] GB/T 700-2006. Carbon structural steels. China Standard Press; Beijing, China; 2006 [in Chinese].

[35] GB/T 228.1-2010. Metallic materials tensile testing at ambient temperature. China Standard Press; Beijing, China; 2010 [in Chinese].

[36] GB 50011－2010. Code for Seismic Design of Buildings. China Ministry of Construction. Beijing, China, 2016 [in Chinese].

[37] Qadir, SJ, Nguyen, VB, Hajirasouliha, I, Ceranic, B, Tracada, E, English, MA. Shape optimisation of cold roll formed sections considering effects of cold working, Thin-Walled Structures. 170 (2022) 108576. https://doi.org/10.1016/j.tws.2021.108576.

[38] ANSI/AISC 341-05, Seismic provisions for structural steel buildings, American Institute of Steel Construction (AISC), Illinois; 2005.

[39] Sabbagh, AB, Petkovski, M, Pilakoutas, K, Mirghaderi, R, Cyclic behaviour of bolted cold-formed steel moment connections: FE modelling including slip, Journal of Constructional Steel Research. 80 (2013) 100-108. https://doi.org/10.1016/j.jcsr.2012.09.010.

[40] E.N. 1998-1, Design of Structures for Earthquake Resistance - Part 1: General Rules, Seismic Actions and Rules for Buildings. CEN, 2005.

[41] FEMA-356, Standard and Commentary for the Seismic Rehabilitation of Buildings, American Society Of Civil Engineers, USA, Virginia, 2000.

[42] Eurocode 3: design of steel structures: Part 1.8: Design of joints, EN 1993-1-8;2005.

[43] K. K. Wijesundara and R. Nascimbene and T. J. Sullivan, Equivalent viscous damping for steel concentrically braced frame structures, Bulletin of Earthquake Engineering. 9 (2011) 1535-1558. https://doi.org/10.1007/s10518-011-9272-4.

[44] N. Yang, Y.N. Zhong, Q.T. Meng, H. Zhang, Hysteretic behaviours of cold-formed steel beam-columns with hollow rectangular section: Experimental and numerical simulations, Thin-Walled Struct. 80 (2014) 217–230. https://doi.org/10.1016/j.tws.2014.03.004